Ore Geology Reviews 140 (2022) 104612

Contents lists available at ScienceDirect

Ore Geology Reviews

journal homepage: www.elsevier.com/locate/oregeorev

Buried Triassic rocks and vertical distribution of ores in the giant Jiaodong gold province (China) revealed by apatite xenocrysts in hydrothermal quartz veins

Hao-Cheng Yu [a], Kun-Feng Qiu [a,*], David Chew [b], Chao Yu [c], Zheng-Jiang Ding [d], Tong Zhou [a], Shuang Li [a], Ke-Fei Sun [a]

[a] State Key Laboratory of Geological Processes and Mineral Resources, School of Earth Sciences and Resources, China University of Geosciences, Beijing 100083, China
[b] Department of Geology, Trinity College Dublin, Dublin 2, Ireland
[c] Jiuqu Gold Mine, Shandong Gold Mining (Linglong) Co., Ltd, Zhaoyuan 265400, China
[d] Shandong Provincial Bureau of Geology & Mineral Resources, Jinan 250013, China

ARTICLE INFO

Keywords:
Apatite geochronology and geochemistry
Xenocryst
Buried rocks
Ore vectoring
Jiaodong

ABSTRACT

Obtaining geological information at depth by lower-cost proxies is important. Apatite grains from hydrothermal quartz veins and their host K-feldspar altered granites from the Jiaodong gold province reveal key insights into the buried rocks and vertical distribution of ores at depth. Two types of apatite grains from hydrothermal quartz veins and their host K-feldspar altered granites are identified. Type I apatite grains in granites coexist with amphibole and feldspar, indicating a magmatic origin. They yield U-Pb Tera–Wasserburg concordia lower intercept dates of 162 ± 13 Ma and 158 ± 9 Ma, which are within uncertainty of zircon U-Pb dates of ca. 160 Ma, representing the crystallization ages for these rocks. Support vector machine (SVM) apatite classification biplots show that the Type I apatite grains have lower LREEs than their I-type granitoid protolith, indicating that LREEs were leached during alteration, which is also suggested by monazite inclusions in altered domains of the Type I apatite. Apatite xenocrysts (Type II) are observed in hydrothermal veins and yield Tera–Wasserburg concordia lower intercept dates of 227 ± 3 Ma and 227 ± 4 Ma. Two subsets of Type II apatite are recognized. SVM apatite classification biplots show that they were derived from the Late Triassic S-type granites and high-grade metamorphic rocks related to the Late Triassic collision between North China and South China blocks. These rocks were less than 11 ± 1 km under the paleosurface during gold mineralization (ca. 120 Ma) estimated by the closure temperature of apatite U-Pb system (460 ± 10 °C), surface temperature at Jiaodong (20 °C), and paleogeothermal gradient (40 ± 5 °C/km). Given the ore-forming paleodepth of about 7 km calculated by previous fluid inclusion works, the unaltered Type II apatite xenocrysts mark that gold ores in the footwall at Jiaodong didn't exceed 4 ± 1 km vertically relative to the sample location. The high preservation potential for apatite in hydrothermal veins illustrates the potential to employ apatite xenocryst as a powerful tool for determining buried rocks at depth.

1. Introduction

Hydrothermal xenocrysts are crystals that are foreign to the hydrothermal system as a whole, which have been incorporated into the hydrothermal fluid from the surrounding host rocks at some point during transport by a physical process (Jerram et al., 2018). They, as well as xenoliths and magmatic xenocrysts, are among the few types of materials that permit direct study of the Earth's upper mantle and deep burial of crustal material (Meisel et al., 2001; Liu et al., 2014; Cao et al., 2019; Qiu et al., 2021b; Wang et al., 2021; Yu et al., 2021b). There has been a rise in interest in studying xenoliths and xenocrysts, promoting the understanding of the formation and evolution of mantle and lower crust (Siebel et al., 2009; Tapster et al., 2014; Li et al., 2020). However, the buried upper crust lacks constraints. Apatite is a common accessory mineral in continental crustal rocks (Hetherington and Harlov, 2008; Chew et al., 2014; Chew and Spikings, 2015; Kusiak et al., 2018; Szopa et al., 2020; Cao et al., 2021; Li et al., 2021; Yu et al., 2021a). Its U-Pb closure temperature varies from 350 °C to c. 570 °C and thus remains

* Corresponding author at: China University of Geosciences, Beijing, No. 29 Xueyuan Road, Haidian District, Beijing 100083, China
E-mail address: kunfengqiu@qq.com (K.-F. Qiu).

https://doi.org/10.1016/j.oregeorev.2021.104612
Received 16 June 2021; Received in revised form 6 November 2021; Accepted 25 November 2021
Available online 29 November 2021

isotopically closed through a hydrothermal fluid but will open through medium- and high-grade metamorphism and magmatism (Chamberlain and Bowring, 2000; Cherniak et al., 1991; Chew and Spikings, 2021; Odlum and Stockli, 2020). This implies the predominance of first-cycle of apatite xenocryst, offering a prime opportunity to reveal signatures of the buried upper crust.

The giant Mesozoic Jiaodong gold province in East China has been estimated to contain up to 5,000 t gold (Fan et al., 2016; Yang et al., 2018; Goldfarb et al., 2019; Deng et al., 2020c; Qiu et al., 2020a). In recent years, mineral exploration has focused on progressively deeper targets as the new surface exposures and shallow deposits are discovered less frequently (Wen et al., 2016; Ma et al., 2017). However, deep drilling programs are expensive and obtaining other lower-cost proxies for the buried rocks and vertical distribution of ores is important. Apatite grains from hydrothermal quartz veins and their host K-feldspar altered granites from the Linglong goldfield in the giant Jiaodong gold province were analyzed by LA–ICP–MS for U–Pb isotope dating and their trace element systematics. In addition, the vertical distribution of the gold mineralization was estimated by the apatite U–Pb closure system and paleogeothermal gradient. These findings confirm that apatite xenocryst is an indicator mineral for revealing buried rocks and furthermore may be used to reveal the vertical distribution of ores.

2. Regional geology of the Jiaodong peninsula

The NE-trending Jiaodong Peninsula is surrounded on three sides by the Yellow Sea and Bohai Sea and to the west by the NNE-striking Tan-Lu fault (Fig. 1). The bedrock geology of the Jiaodong Peninsula is comprised of the Jiaobei terrane in the northwest and the Sulu terrane in the southeast, separated by the NE–trending Wulian–Qingdao–Yantai fault (Goldfarb et al., 2014; Deng et al., 2018; Guo et al., 2020; Sai et al., 2020; Zhang et al., 2020b). The Jiaobei terrane is comprised of the Jiaobei uplift in the north and the Jiaolai basin in the south. Precambrian metamorphic rocks comprise about two-thirds of the exposed bedrock in the Jiaobei uplift (Mills et al., 2015; Deng et al., 2020b; Qiu et al., 2020a). The Sulu terrane in the east Jiaodong peninsula is dominated by ultra-high pressure (UHP) metamorphic rocks, which formed at ca. 245–210 Ma during the Triassic collision between the North China and South China blocks (Dou et al., 2018; Liu et al., 2018).

Widespread intrusions were emplaced into the Precambrian basement terranes and yielded four distinct age peaks: Late Triassic, Late Jurassic, middle Early Cretaceous, and late Early Cretaceous (Fig. 2; Fan et al., 2003; Goldfarb et al., 2019; Deng et al., 2020a). The Late Triassic alkaline granitoid suite was emplaced in small volumes in the southeastern Jiaodong peninsula (Fig. 2). These rocks were emplaced contemporaneously with exhumation following the continental collision (Liu et al., 2017; Zhao et al., 2017). The Late Jurassic (165–145 Ma) granitoids (Linglong suite) together form the largest pluton emplaced into the Precambrian basement across the peninsula (Fan et al., 2016). They are dominantly granite and granodiorite, and their geochemical characteristics indicate that they were most likely derived from partial melting of thickened Archean mafic lower crust without any significant contribution of mantle components (Qiu et al., 2020a). The middle Early Cretaceous (ca. 130–122 Ma) granitoids (Guojialing suite) are dominated by porphyritic granodiorites. These rocks have been suggested to be related to rollback of the Izanagi slab (Goldfarb and Santosh, 2014; Yang et al., 2016; Deng et al., 2020a). The late Early Cretaceous (ca. 119–110 Ma) intrusions (Aishan suite) mainly crop out in the Sulu terrane. They are composed of granodiorite, syenogranite, and monzodiorite. Their adakitic geochemical features suggested that they were derived from partial melting of thickened Neoarchean-Paleoproterozoic lower crust, with weak crust-mantle interaction (Fan et al., 2003; Li et al., 2019).

A thick succession of Mesozoic sedimentary rocks filled the Jiaolai basin, and was deposited on the Precambrian basement. The initiation of the Jiaolai basin was likely caused by transtensional motion along the Tan-Lu fault (Goldfarb et al., 2019; Qiu et al., 2020a). The basin fill consists of fluvial-lacustrine clastic rocks, volcanic rocks, and red beds intercalated with mafic to ultramafic lavas. Abundant flora and fauna and zircon geochronology imply that the succession was deposited in the Cretaceous (Xie et al., 2012; Guo et al., 2017; He et al., 2020).

More than 95% of the Jiaodong gold resource is hosted by Mesozoic granitoids and is controlled by NE- to NNE-trending faults (Yang et al., 2016; Deng et al., 2019; Goldfarb et al., 2019). From west to east, much of the gold resource at Jiaodong is found within the San-Cang, Jiao-Xin, Zhao-Ping, Qi-Peng-Fu, northeast Jiaolai basin, and Mu-Ru gold districts. The ore-bearing zones are characterized by quartz-sericite-pyrite alteration, which partially overprinted earlier K-feldspar alteration (Fan et al., 2016). The ores are mainly divided into disseminated-stockwork type and auriferous quartz vein type (Wen et al., 2015; Guo et al., 2017). Auriferous carbonate vein and breccia types are limited in area and mainly occur in the northeast Jiaolai basin. Much of gold mineralization events occurred at ca. 120 Ma as determined by a variety of different dating methods (Ma et al., 2017; Deng et al., 2020c; Zhang

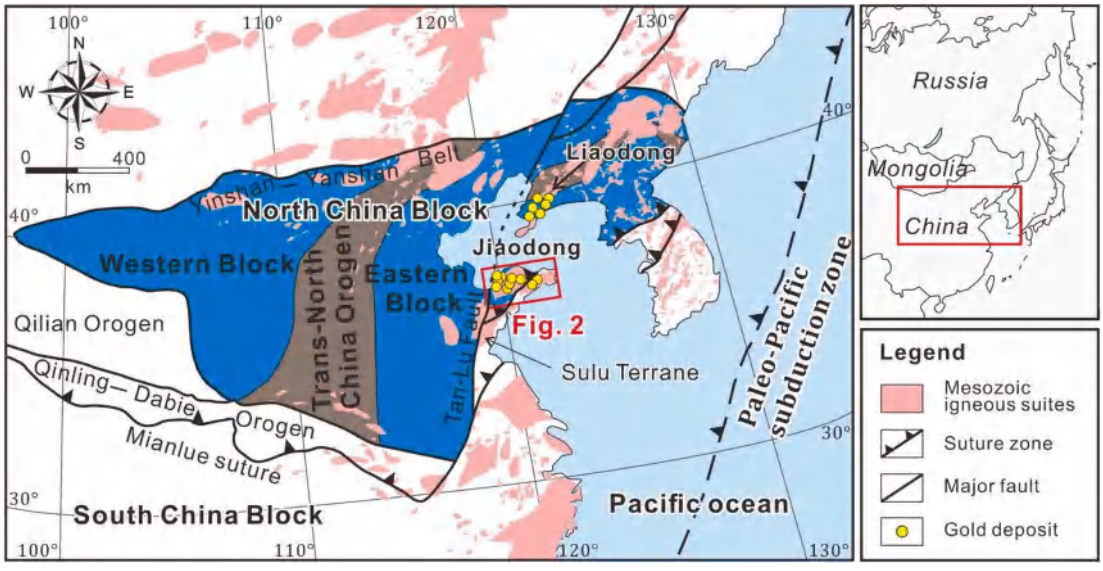

Fig. 1. Simplified geologic map of East Asia showing the location of the Jiaodong gold province. Modified after Qiu et al. (2020b).

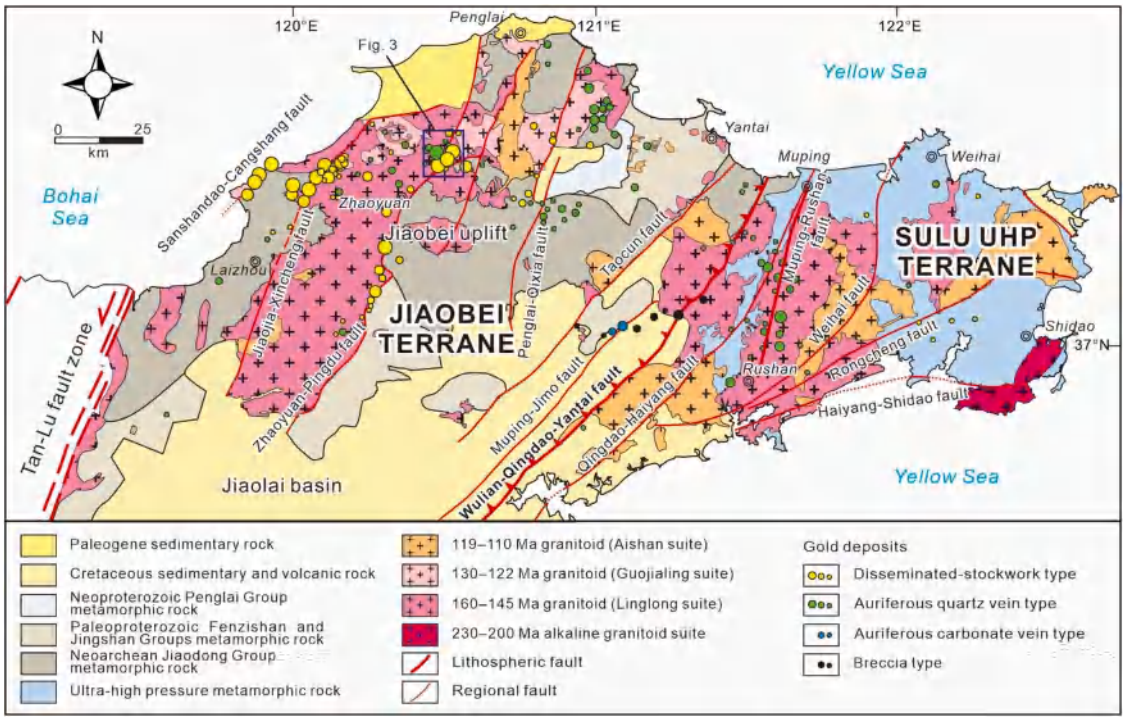

Fig. 2. Simplified geologic map of the giant Jiaodong gold province. Modified after Qiu et al. (2020b).

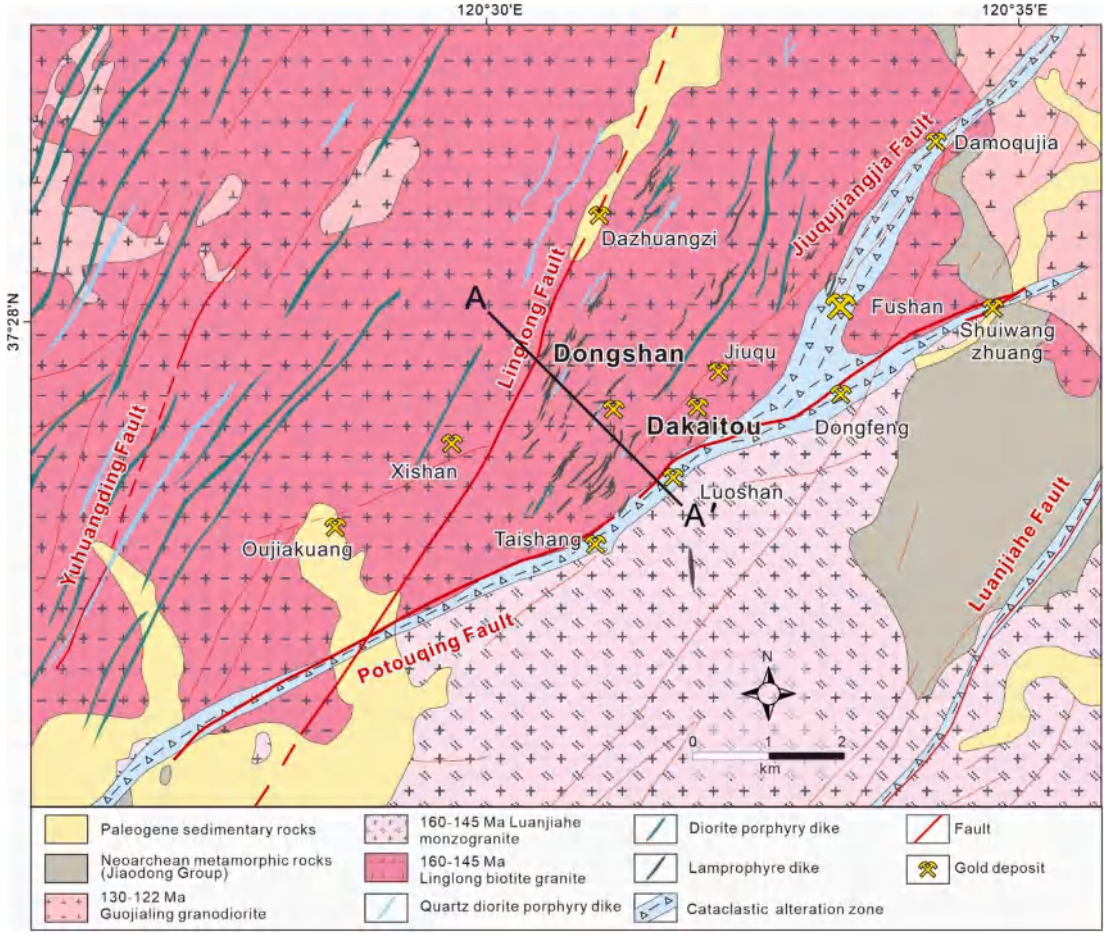

Fig. 3. Simplified geological map of the Linglong goldfield, showing the distribution of major faults and the Dongshan and Dakaitou gold deposits. Modified after Guo et al. (2020).

et al., 2020b). Devolatilization of the subducting Izanagi slab driving substantial volumes of fluids and associated metals along the NE- to NNE-trending faults is potentially the major factor controlling the extensive gold mineralization (Yang et al., 2018; Goldfarb et al., 2019; Qiu et al., 2020a).

3. Local geology of the Linglong goldfield

The Linglong goldfield is located in the north of the Zhao-Ping gold district (Fig. 2). Metamorphic rocks of the Neoarchean Jiaodong Group are exposed in the east of the goldfield, and are dominated by 2.9 to 2.6 Ga tonalite-trondhjemite-granodiorite gneisses (Mills et al., 2015; Qiu et al., 2020a). The most voluminous intrusions in the Linglong goldfield are represented by the Late Jurassic Linglong intrusive suite. The suite was emplaced into the Neoarchean Jiaodong Group and includes the Linglong biotite granite and the Luanjiahe monzonitic granite (Dou et al., 2018). The Early Cretaceous Guojialing porphyritic granodiorite which contains characteristic very coarse K-feldspar phenocrysts was emplaced in the remainder of the region. Numerous NE- to NNE-trending intermediate to mafic dikes, consisting of quartz diorite porphyry, diorite porphyry, and lamprophyre were emplaced into the Linglong suite (Fig. 3). The dikes range in age from 132 to 86 Ma, with a peak at 121 Ma (Deng et al., 2017). The NE-striking Potouqing fault is the main northern branch of the Zhaoyuan-Pingdu fault system. It is more than 15 km long and 40 to 320 m wide, with a dip varying between 28° to 47° SE (Guo et al., 2017). The Jiuqujiangjia fault in the footwall of the Potouqing fault (Fig. 3) is one of a series of secondary faults. The NNE-striking Linglong fault offsets the Potouqing fault and is thus a post-gold late brittle feature (Guo et al., 2020; Qiu et al., 2020a).

The Linglong goldfield comprises more than ten deposits such as Dongshan and Dakaitou, with a total gold resource of ~ 1000 t (Guo et al., 2020; Qiu et al., 2020a). Much of the gold resources are in the footwall of the Potouqing fault and are controlled by a zone of structural complexity (Figs. 3, 4). Gold mineralization is dominated by a series of more than 30 auriferous quartz veins. The veins and related hydrothermal alterations strike to the northeast and dip to the northwest. The alteration is characterized by pinkish K-feldspar alteration forming an outer halo and quartz-pyrite-sericite alteration forming an inner halo (Fig. 5). The ore minerals are primarily pyrite, with lesser chalcopyrite, galena, sphalerite, and native gold. The gangue minerals mainly consist of quartz, sericite, K-feldspar, and calcite.

4. Sampling and analytical procedures

4.1. Sample description

Four representative samples of the Linglong granites with K-feldspar alteration (two samples) and hydrothermal quartz veins (two samples) were collected from the Dongshan and Dakaitou deposits in the Linglong goldfield (Table 1). The sample locations are marked on Figs. 4 and 5. The pinkish to yellowish K-feldspar altered Linglong granite samples (DS01 and DKT01) are characterized by stockwork and disseminated structures (Fig. 6A, C). The main minerals are quartz, plagioclase, amphibole, biotite, K-feldspar, sericite, and chlorite, with minor monazite-(Ce) and hematite (Figs. 6-9). Amphibole is dominated by pargasite (Sai et al., 2016) and is partially chloritized (Fig. 9A). K-feldspar occurs as variously sized patchy shapes from 20 to 600 μm wide (Fig. 7A) with a chemical composition of Or_{91} to Or_{98} (Wang et al., 2020). Monazite-(Ce) grains occur in clusters associated with sericite or occur as inclusions in apatite (Fig. 9A). The gray quartz-sulfide-gold hydrothermal vein samples (DS02 and DKT02) are mainly composed of quartz, pyrite, and sericite (Figs. 6B, D; 7B).

4.2. Mineral separation

Mineral separation was conducted at the Langfang Chengxin Geological Service Co., Hebei Province, China. Mineral separation employed conventional sieving followed by magnetic and heavy liquid separation methods. Zircon and apatite separates were handpicked and were mounted in epoxy resin and polished down to near half thickness to expose internal structures. Polished mounts were then carbon coated for cathodoluminescence (CL) imaging using a JXA-8800 scanning electron microscope at the Langfang Chengxin Geological Service Co., Hebei Province, China, and a Tescan GAIA 3 electron microscope at the Analytical Laboratory of the Beijing Research Institute of Uranium Geology, Beijing, China. The detailed operating conditions were provided in Yu et al. (2020).

4.3. Electron probe micro-analysis of apatite

Electron probe micro-analysis (EPMA) on apatite were carried out at the Shandong Key Laboratory of Geological Processes and Resource Utilization in Metallic Minerals, Shandong Geological Sciences Institute, China, with a JEOL JXA-8230 Electron Probe Micro Analyzer. The analytical conditions employed an accelerating voltage of 15 kV, a beam current of 20 nA, and a beam diameter of 1–5 μm. The full analytical procedures were provided in Qiu et al. (2019).

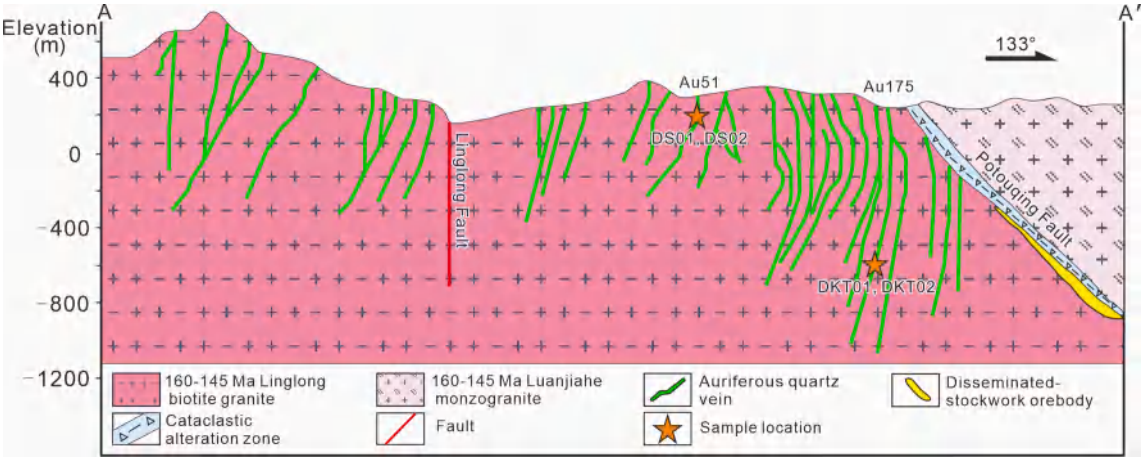

Fig. 4. Geological profile across the orebodies of the Linglong goldfield, showing the sample locations. Modified after Wen et al. (2015).

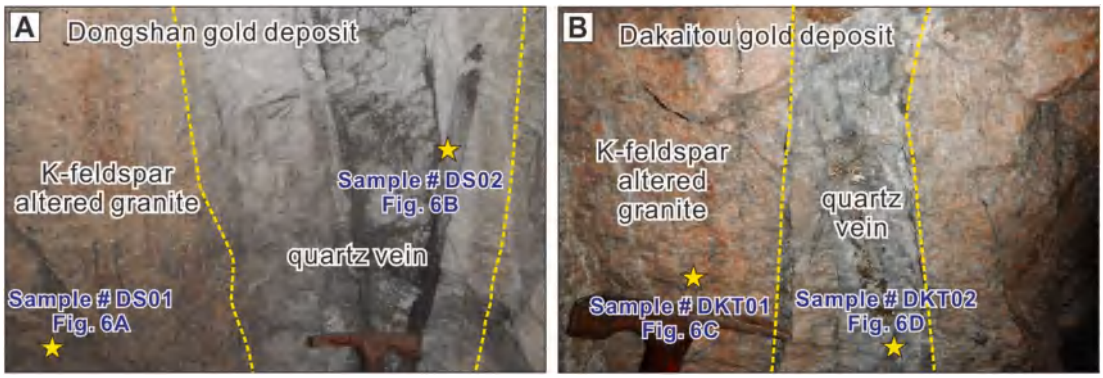

Fig. 5. Field photographs showing the alteration, ore and mineral assemblages at the Dongshan (A) and Dakaitou (B) gold deposits.

Table 1
Summary of sample information.

No.	Location	Lithology	Texture of apatite	Age of apatite	Origin of apatite
DS01	Au 51 orebody; 206 m level	K-feldspar altered granite	Anhedral	162 ± 13 Ma	I-type granite
DS02	Au 51 orebody; 206 m level	Quartz vein	Euhedral	227 ± 3 Ma	S-type granite and high-grade metamorphic rocks
DKT01	Au 175–8 orebody; −620 m level	K-feldspar altered granite	Anhedral	158 ± 9 Ma	I-type granite
DKT02	Au 175–8 orebody; −620 m level	Quartz vein	Euhedral	227 ± 4 Ma	S-type granite and high-grade metamorphic rocks

4.4. Zircon and apatite LA–ICP–MS U–Pb dating and trace element analyses

Zircon U–Pb isotope analyses were conducted by LA–ICP–MS at the Isotopic Laboratory, Tianjin Center, China Geological Survey using a Neptune double focusing multiple-collector coupled to a NEW WAVE 193 nm-FX ArF Excimer laser-ablation system. The detailed operating conditions and data reduction procedures follow those described in Geng et al. (2017) and Yu et al. (2021a). 91500 zircon (Wiedenbeck et al., 1995) and Plešovice zircon (Sláma et al., 2008) were used as the age reference materials. Apatite U–Pb isotope and trace element analyses were conducted by LA–ICP–MS at the Isotopic Laboratory, Tianjin Center, China Geological Survey, Tianjin, China and Yanduzhongshi Geological Analysis Laboratories Ltd., Beijing, China using an Agilent 7900 ICP–MS and an Analytik Jena M90 quadrupole ICP–MS coupled to a NEW WAVE 193 nm-FX ArF Excimer laser-ablation system, respectively. Otter Lake apatite (Barfod et al., 2005) and MAD2 apatite (Cochrane et al., 2014) were used as the age reference materials for apatite U–Pb geochronology analyses. The NIST SRM 610 and 612 reference material glasses were used as an external reference material for trace element determinations on zircon and apatite, respectively. The internal element standard isotope was ^{44}Ca for apatite trace element analyses. Age calculations and concordia plots were reported at the 2σ uncertainty level and were processed using the Isoplot software (version 3.75; Ludwig, 2012). The downhole fractionation, instrument drift and mass bias correction factors for Pb/U ratios on apatite follow those described in Chew et al. (2011).

5. Analytical results and interpretations

5.1. Zircon morphology and LA–ICP–MS U–Pb dates

The zircon morphology and U–Pb dating results are illustrated in Fig. 8 and presented in supplementary table 1. Most zircon separates from K-feldspar altered Linglong granite (DS01 and DKT01) are pristine and euhedral and display well-developed oscillatory, lengthwise, and sector growth zoning, revealing a magmatic origin (Fig. 8A; Yu et al., 2021a). The crystals have lengths of 80–200 μm and length/width ratios of 2 to 4. The crystallization age of the Linglong granite is determined by 14 concordant dates from sample DS01 and 12 concordant dates from sample DKT01. The DS01 dates show Th and U contents of 28 to 285 ppm and 44 to 600 ppm, with Th/U ratios ranging from 0.38 to 1.21, and yield a weighted mean ^{206}Pb/^{238}U date of 163.4 ± 1.7 Ma (MSWD = 2.6; Fig. 8B, C). The DKT01 analyses show Th and U contents of 5 to 1397 ppm and 99 to 1477 ppm, with Th/U ratios ranging from 0.04 to 0.95, and yield a weighted mean ^{206}Pb/^{238}U date of 158.1 ± 1.5 Ma (MSWD = 0.8; Fig. 8D, E). The small spread along concordia in both samples DS01 and DKT01 may indicate minor Pb loss associated with hydrothermal alteration. Several crystals from sample DKT01 have CL-dark rim overgrowths. They have high Th and U contents of 415 to 1491 ppm and 891 to 3175 ppm and yield apparently young ^{206}Pb/^{238}U date of 130–121 Ma (Fig. 8D). These results are close with the gold mineralization events that occurred at ca. 120 Ma (Qiu et al., 2020a), suggesting that these zircon overgrowths were contemporaneous with mineralization. Some grains have rounded margins or occur as cores surrounded by magmatic rims, suggesting that they were inherited from the melt source or captured by the rising magma (Fig. 8A). The ages of the inherited zircon show peaks of Paleoproterozoic, Neoproterozoic, and Late Triassic to Early Jurassic age (Fig. 8A).

5.2. Apatite morphology, LA–ICP–MS U–Pb dates and composition

Two types of apatite grains are observed in this study. Type I apatite grains separated from the K-feldspar altered Linglong granites (DS01 and DKT01) are anhedral. They vary from 80 to 200 μm in length, with length/width ratios between 1 and 2 (Fig. 9A). The crystals commonly show textures indicative of fluid metasomatism under CL imaging. The unaltered domains are more homogeneous than the altered domains. The altered grains are characterized by pitted surfaces with visible voids and mineral inclusions and cracks (Fig. 9A). Thirty U–Pb isotope analyses from sample DKT01 lie on an unanchored line with a lower intercept date of 158 ± 9 Ma (MSWD = 0.65) on Tera-Wasserburg diagrams. Thirty-one analyses from sample DS01 yield a lower intercept date of 162 ± 13 Ma (MSWD = 1.5) anchored using a ^{207}Pb/^{206}Pb value of 0.946 from the Tera-Wasserburg concordia of the sample DKT01 (supplementary table 2; Fig. 9C, D). All Type I apatite grains are fluorapatite (supplementary table 3). They show low U and Th contents,

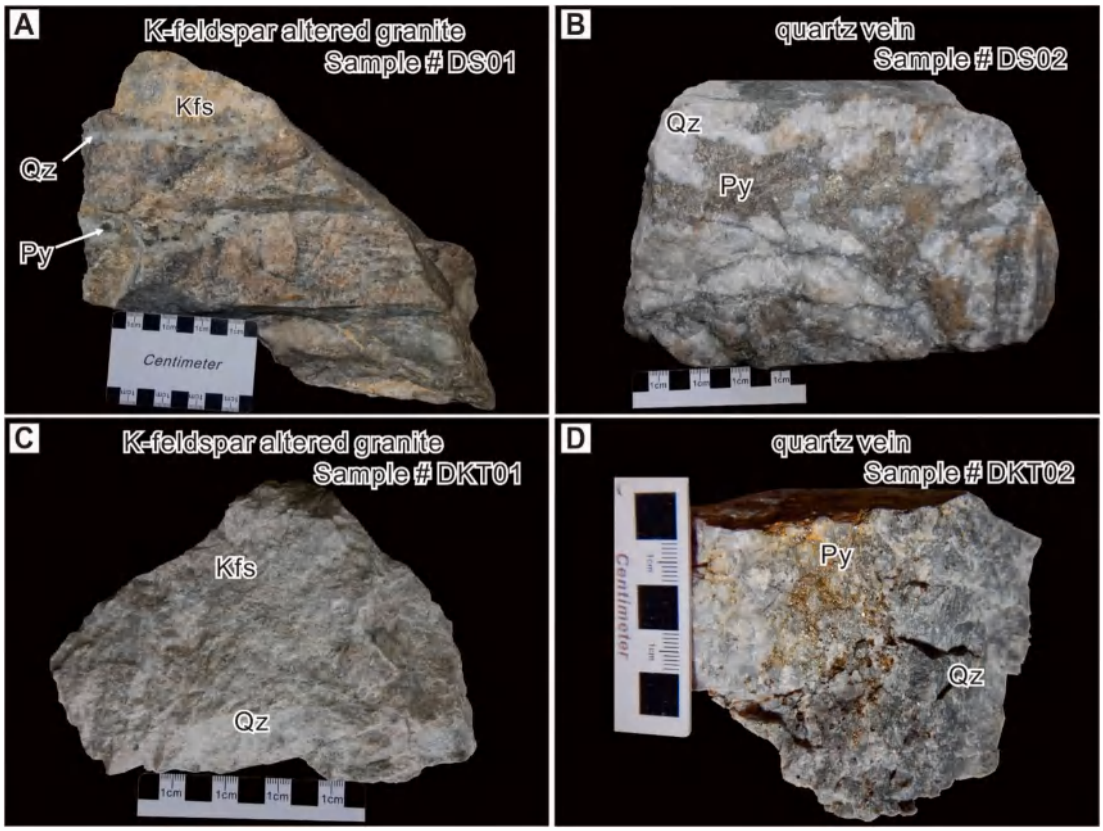

Fig. 6. Hand specimen of K-feldspar altered Linglong granite (A) and a hydrothermal quartz vein (B) at Dongshan. Hand specimen of K-feldspar altered Linglong granite (C) and a hydrothermal quartz vein (D) at Dakaitou. Kfs = K-feldspar, Py = pyrite, Qz = quartz. Mineral abbreviations refer to Whitney and Evans (2010).

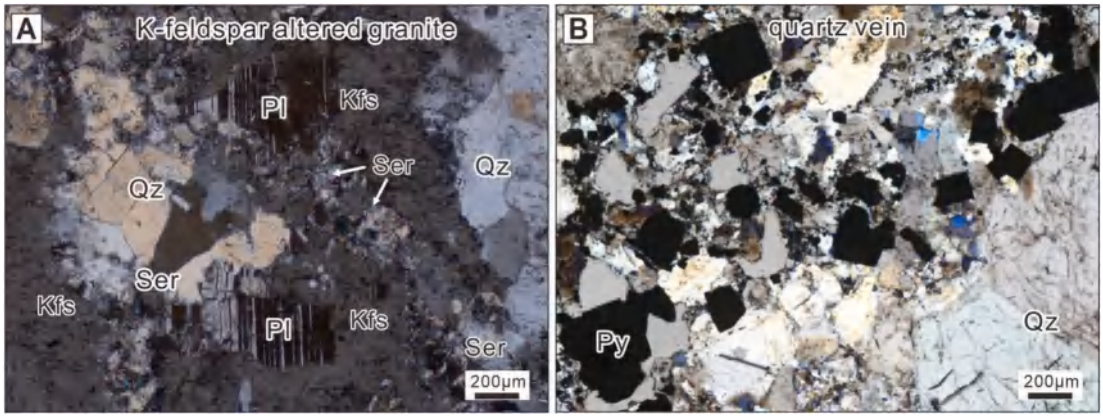

Fig. 7. Photomicrographs of the K-feldspar altered Linglong granite (A) and hydrothermal quartz vein (B). Ser = sericite.

with average Th and U contents of 11 ppm and 15 ppm. They exhibit Sr and Y contents ranging from 488 to 633 ppm and 1090 to 2600 ppm, with a mean Sr/Y ratio of 0.39. Their light rare earth element (LREE) concentrations are 680 to 2323 ppm (supplementary table 4; Fig. 9G).

Euhedral and pristine Type II apatite grains were observed in the hydrothermal quartz vein samples (DS02 and DKT02) (Fig. 9B). They are 50 to 200 μm in length, with length/width ratios between 2 and 4. Some grains show weak oscillatory growth zoning under CL imaging. Type II apatite crystals are further divided into two subtypes. The more abundant Type IIa apatite grains are characterized by green to blue colors on false-color CL images. The Type IIb apatite grains show bright orange-red color on false-color CL images (Fig. 9B). These two subtypes define a well-constrained mixing line between the radiogenic and the common Pb components. Apatite crystals from samples DS02 and DKT02 yield lower intercept dates of 227 ± 3 Ma (MSWD = 2.2, n = 44; Fig. 9E) and 227 ± 4 Ma (MSWD = 0.51, n = 57; Fig. 9F) on a Tera-Wasserburg diagram. The lower intercept was anchored using a $^{207}Pb/^{206}Pb$ value of 0.851 derived from the terrestrial Pb evolution model (Stacey and Kramers, 1975). All types IIa and IIb apatite grains are fluorapatite (supplementary table 3). The average Th and U contents of types IIa and IIb apatite grains are 26 ppm and 19 ppm, and 34 ppm and 48 ppm respectively. The Sr contents of types IIa and IIb apatite grains are in the range of 31–44 ppm and 117–137 ppm and their Y contents vary from 2290 to 4530 ppm and 1230–3800 ppm, with average Sr/Y ratios of 0.01 and 0.06, respectively (supplementary table 4; Fig. 9G).

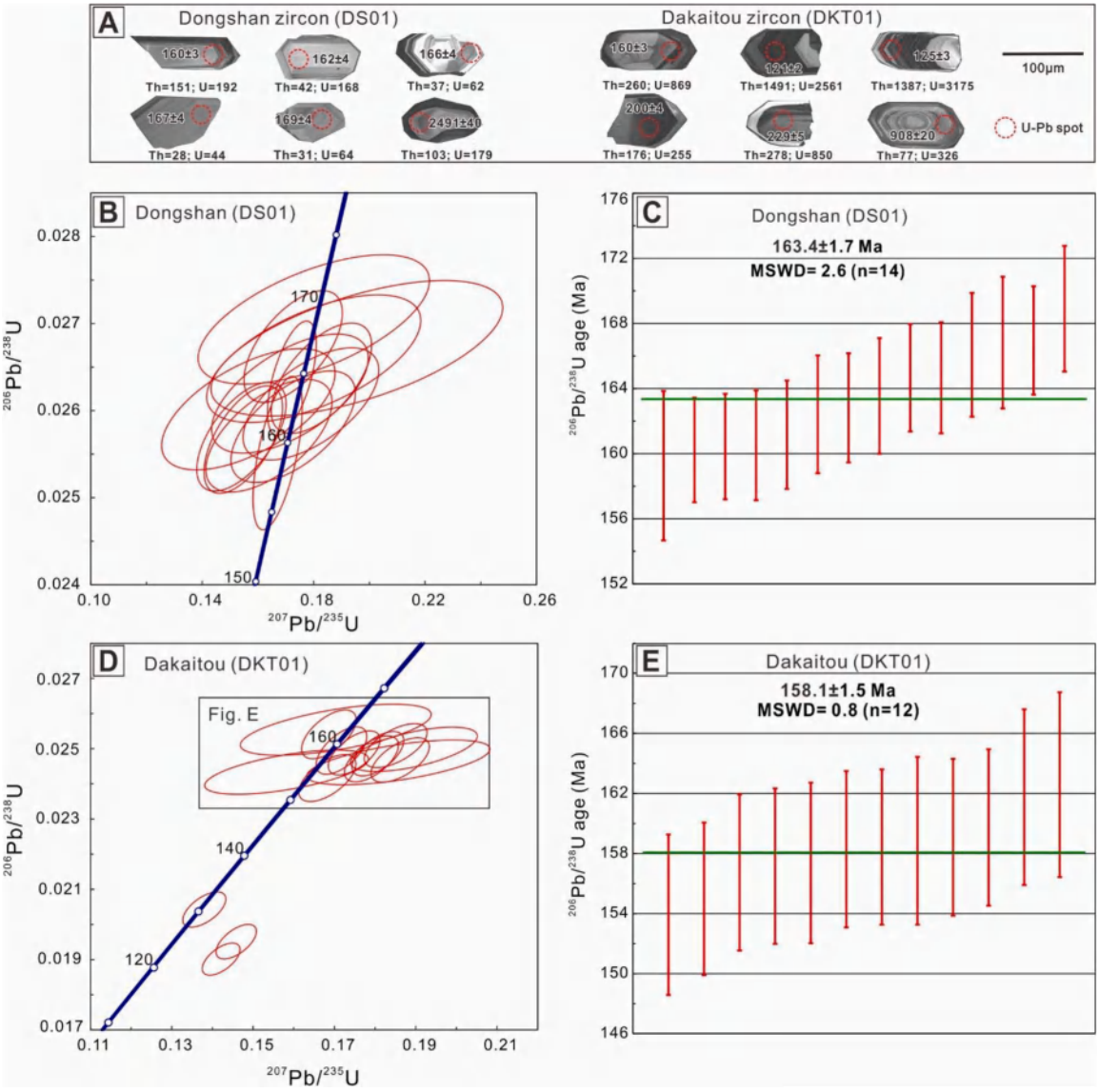

Fig. 8. (A) CL images showing the morphology and internal textures in zircon from the Dongshan and Dakaitou samples. Wetherill concordia plots and weighted mean $^{206}Pb/^{238}U$ ages for zircon U-Pb analyses from the K-feldspar altered Linglong granite at Dongshan (B, C) and Dakaitou (D, E).

6. Discussion

6.1. Origins of apatite

Apatite in this study can be divided into two types based on their texture, geochronology, and composition. The anhedral rounded apatite (Type I) in K-feldspar altered Linglong granite coexists with biotite, amphibole, and plagioclase or K-feldspar and thus is interpreted as a magmatic origin (Fig. 9A). They yield lower intercept dates of 162 ± 13 Ma and 158 ± 9 Ma (Fig. 9C, D), which are consistent with the zircon U–Pb dates of 163.4 ± 1.7 Ma and 158.1 ± 1.5 Ma (Fig. 8) obtained from the same samples, confirming that the Type I apatite was originally primary magmatic (Fig. 10A). The textures of fluid metasomatism in Type I apatite reveal extensive metasomatic alteration. Sharp boundaries between the unaltered and the altered domains and abundant fluid inclusions in the altered domains suggest a dissolution-reprecipitation process associated with K-feldspar alteration at 300 to 500 ℃ by fluid inclusion thermometry (Zeng et al., 2016; Wang et al., 2020). Although the altered domains record the conditions of the metasomatic fluids, pervasive micro-porosities and fluid inclusions prevent us from gaining robust fluid information using LA–ICP–MS. The support vector machine apatite classification biplot shows that the LREEs of Type I apatite from Linglong I-type granite are lower than typical I-type granitoids and trend toward the low- and medium-grade metamorphic and metasomatic fields (O'Sullivan et al., 2020). This indicates that apatite chemical composition can be modified by hydrothermal fluids (Zeng et al., 2016; Cao et al., 2019). REE-bearing mineral inclusions (e.g., monazite) within the altered domains of Type I apatite indicate that the leached REEs and Y immediately reprecipitated (Fig. 9A).

The euhedral and pristine apatite (Type II) only appears in quartz-sericite-pyrite vein samples (Fig. 9B), which implies that the Type II apatite has no genetic relationship with the host granite. There are two possible hypotheses for its origin: hydrothermal or captured. The hydrothermal hypothesis is easy to rule out because the ca. 227 Ma crystallization ages of Type II apatite (Fig. 9E, F) are much older than the emplacement of the host granite at ca. 160 Ma and the gold mineralization at ca. 120 Ma. As a result, the Type II apatite is interpreted as xenocrysts captured from rocks below the Linglong granite by hydrothermal quartz veins. The textural, compositional, and geochronological evidence acquired during this study, further divided Type II apatite grains into two subtypes. The Type IIa apatite originates from S-type granites based on the support vector machine apatite classification

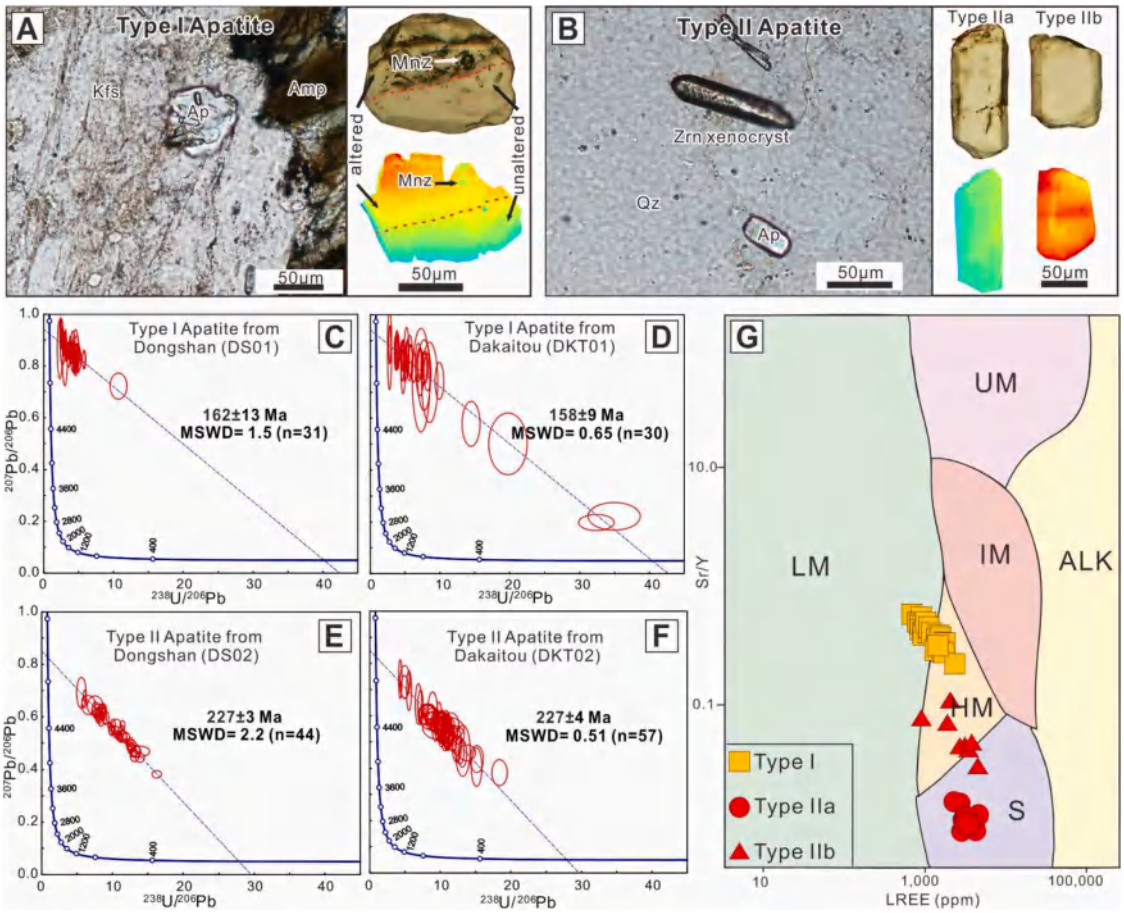

Fig. 9. Photomicrographs and diagrams showing apatite internal textures, U-Pb age data and trace element composition. (A) Type I apatite in K-feldspar altered Linglong granite, showing textures consist with metasomatism. (B) Type II apatite in hydrothermal quartz veins with two subtypes. (C) Tera-Wasserburg concordia plots for U-Pb analyses of Type I apatite. (D) Tera-Wasserburg concordia plots for U-Pb analyses of Type II apatite. (E) Apatites plotted on a support vector machine apatite classification diagram (Sr/Y vs LREE [La, Ce, Pr, Nd]) (after O'Sullivan and Chew, 2020). ALK = alkaline-rich igneous, HM = high-grade metamorphic, IM = I-type granitoids and mafic igneous, LM = low- and medium-grade metamorphic and metasomatic, S = S-type granites, UM = ultramafic igneous. Amp = amphibole, Ap = apatite, Mnz = monazite, Zrn = zircon. Mineral abbreviations refer to Whitney and Evans (2010).

diagram (Fig. 9G; O'Sullivan and Chew, 2020). Most Type IIb apatite crystals plot in the high-grade metamorphic field, indicating that they are most likely derived from high-grade metamorphic rocks. U–Pb dates of both type IIa and IIb apatite grains at ca. 227 Ma imply that they both crystallized in the Late Triassic. This is also consistent with the abundant Late Triassic magmatic and metamorphic zircon xenocrysts in the Linglong granite (Huang et al., 2014).

6.2. *Nature and location of the apatite xenocryst sources*

The Late Triassic has been recognized as a critical period for East China, during which the North China and South China blocks collided followed the initiation of lithospheric thinning of North China block might begin (Li et al., 2019; Qiu et al., 2021a). The Late Triassic apatite xenocrysts therefore could derive from (1) collision between North China and South China blocks and/or (2) lithospheric thinning of North China block. Late Triassic rocks are not exposed in the Jiaobei terrane but exposed in the Liaodong Peninsula, the Sulu terrane, the Dabie orogen, and the Qinling orogen (Fig. 1; Qiu et al., 2020b). The Late Triassic intrusive rocks emplaced at ca. 220–211 Ma at Liaodong Peninsula were considered to be related to lithospheric thinning of North China block (Duan et al., 2014; Quan et al., 2020). Geochemical characteristics indicate that they are mainly composed of I–type and A–type granitoids and mafic dikes (Quan et al., 2020). This contradicts our apatite results, indicating that the apatite xenocrysts are unlikely to be related to the lithospheric thinning of North China block. Late Triassic alkaline complex emplaced at 213–210 Ma crops out along the far southeastern edge of the Jiaodong Peninsula (Xu et al., 2016). They belong to the A2-type granites contemporaneously with exhumation following continental collision (Zhao et al., 2017), which is ruled out the possibility of the apatite source. The Sulu-Dabie area is one of the largest and best-exposed UHP metamorphic belts in the world. Zircon and titanite U–Pb dating showed that the partial melting process of UHP rocks had two major episodes at ca. 230–224 Ma and 220–215 Ma (Zhao et al., 2020). In addition, Late Triassic (ca. 210 Ma) S-type granites related to Late Triassic collisional orogeny between North China and South China blocks crop out in the Qinling orogen (Yang et al., 2015; Lu et al., 2016). As a result, although the Late Triassic S-type granites or high-grade metamorphic rocks are not exposed in the Jiaobei terrane, the apatite xenocrysts most likely originate from buried rocks in the Jiaobei terrane associated with the collision between North China and South China blocks (Fig. 10A).

As discussed above, the apatite grains were xenocrysts in origin captured in auriferous quartz vein. This suggests that the ore-forming fluids and the apatite sources shared a same path at depth. The Potouqing fault controls the gold mineralization at Linglong goldfield (Figs. 3, 10) and therefore is considered as the path of the ore-forming fluids with apatite xenocrysts. This means that the apatite source was below the Linglong granite and the temperature was below the closure temperature of the apatite U–Pb system at ca. 120 Ma. The Pb diffusion

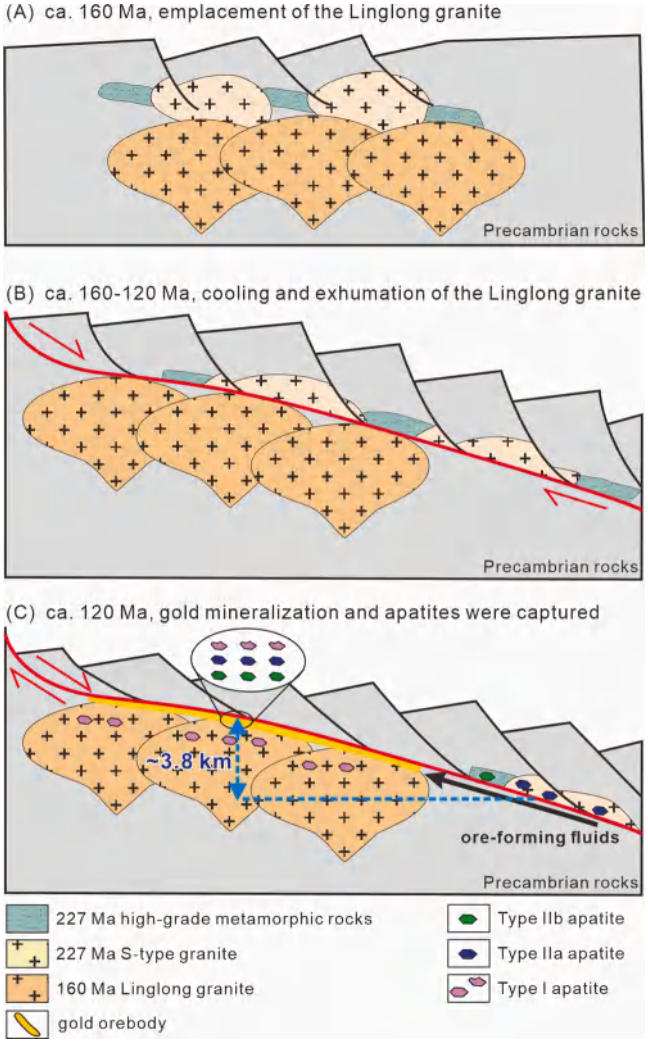

Fig. 10. Schematic cross sections illustrating the relative spatial relationship of the Linglong granite and geology at depth (modified from Yang et al., 2016). (A) Linglong granites emplaced at ca. 160 Ma; (B) Cooling and exhumation of the Linglong granites from ca. 160–120 Ma; (C) Hydrothermal quartz veins captured apatite xenocrysts at ca. 120 Ma.

parameters were controlled by effective diffusive radius and cooling rate (Dodson, 1973; Cherniak et al., 1991). The apatite xenocrysts are typically 100 μm in size (Fig. 9). Yang et al. (2016) and Zhang et al. (2020a, b) calculated the cooling rate at Jiaobei terrane as 2–5 °C/Ma. The apatite U–Pb closure temperature is thus estimated at c. 460 ± 10 °C (Chamberlain and Bowring, 2000). The surface temperature at Jiaodong has been estimated at c. 20 °C by Zhang et al. (2020a) and Sai et al. (2020). The peak of lithospheric thinning of North China block occurred at the Early Cretaceous and resulted in a significant high geothermal gradient (Qiu et al., 2014; Ren et al., 2020). A paleogeothermal gradient of 40 ± 5 °C/km was calculated by Qiu et al. (2014) and Ren et al. (2020) using vitrinite reflectance and apatite fission track. Previous fluid inclusion work at Jiaodong showed that the temperature of the ore-forming fluids remains nearly the same over vertical depth interval (Hu et al., 2013; Wen et al., 2016). This indicates that the hydrothermal fluids have little heating effect on the wall rock. As a result, the apatite xenocryst source was no more than c. 11 ± 1 km under the paleo-surface at ca. 120 Ma. Based on ductile shear deformation in the Linglong granite, Dou et al. (2018) proposed that the depth of Linglong granite was ~10–15 km. This rules out the possibility that the apatite xenocryst source was in the footwall of the Potouqing fault, as the apatite U–Pb system would likely have been reset. As a result, the apatite xenocryst source was likely located in the hanging wall of the Potouqing fault system (Fig. 10A, B).

6.3. Implications on vertical distribution of ores at Jiaodong

Thousands of tons of gold resources at Jiaodong are controlled by NE- to NNE-trending faults and are hosted in the Mesozoic granitoids in the footwall of the faults (Deng et al., 2020a; Qiu et al., 2020a). Low temperature thermochronology indicates that the Jiaodong gold deposits are partially eroded but relatively well preserved, with great gold endowment potential (Liu et al., 2017; Zhang et al., 2020a). Exploration for potentially deep orebodies in the footwall is being undertaken by drilling of increasingly deep drill holes. Compared to the Type I apatite crystals, most of which are altered by the hydrothermal fluids, no altered Type II apatite grains are observed. This result suggests that the apatite xenocryst source beneath the Linglong granite is unaltered and thus gold mineralization in the footwall did not exceed c. 11 ± 1 km depth under the paleo-surface at ca. 120 Ma (Fig. 10C). Gold mineralization in Linglong likely occurred at a depth of c. 7 km (Guo et al., 2020). The apatite xenocryst source was therefore estimated at less than c. 4 ± 1 km beneath the sampled Linglong granite, marking that gold mineralization in the footwall at Linglong didn't exceed 4 ± 1 km vertically (Fig. 10C).

7. Conclusion

Two types of apatite are observed in hydrothermal quartz veins and their host granites which have undergone K-feldspar alteration in the giant Jiaodong gold province. Type I apatite crystals in the altered granite are magmatic in origin. Their metasomatism textures and decrease in REEs and Y indicated dissolution-reprecipitation processes during K-feldspar alteration. Type II apatite crystals are only observed in hydrothermal quartz veins. They are derived from Late Triassic S-type granites and Late Triassic high-grade metamorphic rocks which are likely related to the Late Triassic collision between North China and South China blocks. The Type II apatite crystals are thus likely xenocrysts derived from unaltered Late Triassic S-type granites and Late Triassic high-grade metamorphic rocks beneath the exposed granite. The apatite xenocryst source in the hanging wall of the Potouqing normal fault was less than 4 ± 1 km below the Linglong granite at 120 Ma as estimated by the closure temperature of apatite U–Pb system and the paleogeothermal gradient. The unaltered buried rocks mark that gold mineralization in the footwall at Linglong didn't exceed 4 ± 1 km vertically. This study demonstrates that apatite xenocrysts captured by hydrothermal vein represent a powerful tool for determining buried rocks underground by integrating texture, geochronology, and geochemistry.

Declaration of Competing Interest

The authors declare that they have no known competing financial interests or personal relationships that could have appeared to influence the work reported in this paper.

Acknowledgements

We thank Ji-Chun Wu, Fei Liu, Zhen Zhang, and Zhao-Yuan Xu at Shandong Gold Mining for assistance during the field trip. This research was financially supported by the National Key Research Program (2019YFA0708603), the National Natural Science Foundation of China (42130801, 42072087, 42111530124, 41973048), the Beijing Nova Program (Z201100006820097), and the 111 Project of the Ministry of Science and Technology (BP0719021).

Appendix A. Supplementary data

Supplementary data to this article can be found online at https://doi.

org/10.1016/j.oregeorev.2021.104612.

References

Barfod, G.H., Krogstad, E.J., Frei, R., Albarède, F., 2005. Lu–Hf and PbSL geochronology of apatites from Proterozoic terranes: A first look at Lu–Hf isotopic closure in metamorphic apatite. Geochim. Cosmochim. Acta 69 (7), 1847–1859.

Cao, M.J., Evans, N.J., Hollings, P., Cooke, D.R., McInnes, B.I., Qin, K., 2021. Apatite Texture, Composition, and O-Sr-Nd Isotope Signatures Record Magmatic and Hydrothermal Fluid Characteristics at the Black Mountain Porphyry Deposit, Philippines. Econ. Geol.

Cao, M., Evans, N.J., Qin, K., Danišík, M., Li, G., McInnes, B.I.A., 2019. Open apatite Sr isotopic system in low–temperature hydrous regimes. J. Geophys. Res.: Solid Earth 124 (11), 11192–11203.

Chamberlain, K.R., Bowring, S.A., 2000. Apatite–feldspar U-Pb thermochronometer: a reliable, mid-range (~ 450° C), diffusion-controlled system. Chem. Geol. 172 (1–2), 173–200.

Cherniak, D.J., Lanford, W.A., Ryerson, F.J., 1991. Lead diffusion in apatite and zircon using ion implantation and Rutherford backscattering techniques. Geochim. Cosmochim. Acta 55 (6), 1663–1673.

Chew, D.M., Petrus, J.A., Kamber, B.S., 2014. U-Pb LA–ICPMS dating using accessory mineral standards with variable common Pb. Chem. Geol. 363, 185–199.

Chew, D.M., Spikings, R.A., 2015. Geochronology and Thermochronology Using Apatite: Time and Temperature, Lower Crust to Surface. Elements 11 (3), 189–194.

Chew, D.M., Spikings, R.A., 2021. Apatite U-Pb Thermochronology: A Review. Minerals 11 (10), 1095. https://doi.org/10.3390/min11101095.

Chew, D.M., Sylvester, P.J., Tubrett, M.N., 2011. U-Pb and Th–Pb dating of apatite by LA–ICPMS. Chem. Geol. 280 (1-2), 200–216.

Cochrane, R., Spikings, R.A., Chew, D., Wotzlaw, J.F., Chiaradia, M., Tyrrell, S., Schaltegger, U., Van der Lelij, R., 2014. High temperature (> 350 C) thermochronology and mechanisms of Pb loss in apatite. Geochim. Cosmochim. Acta 127, 39–56.

Deng, J., Qiu, K.F., Wang, Q.F., Goldfarb, R., Yang, L.Q., Zi, J.W., Geng, J.Z., Ma, Y., 2020a. In Situ dating of hydrothermal monazite and implications for the geodynamic controls on ore formation in the Jiaodong gold Province, eastern China. Econ. Geol. 115, 671–685.

Deng, J., Wang, C., Bagas, L., Santosh, M., Yao, E., 2018. Crustal architecture and metallogenesis in the south-eastern North China Craton. Earth Sci. Rev. 182, 251–272.

Deng, J., Wang, Q., Li, G., 2017. Tectonic evolution, superimposed orogeny, and composite metallogenic system in China. Gondwana Res. 50, 216–266.

Deng, J., Wang, Q., Santosh, M., Liu, X., Liang, Y., Yang, L., Zhao, R., Yang, L., 2020b. Remobilization of metasomatized mantle lithosphere: a new model for the Jiaodong gold province, eastern China. Mineral. Deposita 55 (2), 257–274.

Deng, J., Yang, L.-Q., Groves, D.I., Zhang, L., Qiu, K.-F., Wang, Q.-F., 2020c. An integrated mineral system model for the gold deposits of the giant Jiaodong province, eastern China. Earth Sci. Rev. 208, 103274. https://doi.org/10.1016/j.earscirev.2020.103274.

Deng, J., Zhai, Y., Mo, X., Wang, Q., 2019. Temporal-spatial distribution of metallic ore deposits in China and their geodynamic settings. Soc. Econ. Geol. 22, 103–132.

Dodson, M.H., 1973. Closure temperature in cooling geochronological and petrological systems. Contrib. Mineral. Petrol. 40 (3), 259–274.

Dou, J.Z., Zhang, H.-F., Tong, Y., Wang, F., Chen, F.K., Li, S.R., 2018. Application of geothermo-barometers to Mesozoic granitoids in the Jiaodong Peninsula, eastern China: Criteria for selecting methods of pressure estimation and implications for crustal exhumation. J. Asian Earth Sci. 160, 271–286.

Duan, X., Zeng, Q., Yang, J., Liu, J., Wang, Y., Zhou, L., 2014. Geochronology, geochemistry and Hf isotope of Late Triassic magmatic rocks of Qingchengzi district in Liaodong peninsula, Northeast China. J. Asian Earth Sci. 91, 107–124.

Fan, H.R., Feng, K., Li, X.H., Hu, F.F., Yang, K.F., 2016. Mesozoic gold mineralization in the Jiaodong and Korean peninsulas. Acta Petrol. Sin. 32, 3225–3238.

Fan, H.R., Zhai, M.G., Xie, Y.H., Yang, J.H., 2003. Ore-forming fluids associated with granite-hosted gold mineralization at the Sanshandao deposit, Jiaodong gold province. China. Mineral. Deposita 38 (6), 739–750.

Geng, J.Z., Qiu, K.F., Gou, Z.Y., Yu, H.C., 2017. Tectonic regime switchover of Triassic Western Qinling Orogen: Constraints from LA-ICP-MS zircon U-Pb geochronology and Lu–Hf isotope of Dangchuan intrusive complex in Gansu, China. Geochemistry 77 (4), 637–651.

Goldfarb, R., Qiu, K.F., Deng, J., Chen, Y.J., Yang, L.Q., 2019. Orogenic gold deposits of China. Society of Economic Geologists Special Publications 22, 263–324.

Goldfarb, R.J., Santosh, M., 2014. The dilemma of the Jiaodong gold deposits: Are they unique? Geosci. Front. 5 (2), 139–153.

Goldfarb, R.J., Taylor, R.D., Collins, G.S., Goryachev, N.A., Orlandini, O.F., 2014. Phanerozoic continental growth and gold metallogeny of Asia. Gondwana Res. 25 (1), 48–102.

Guo, L.N., Deng, J., Yang, L.Q., Wang, Z.L., Wang, S.R., Wei, Y.J., Chen, B.H., 2020. Gold deposition and resource potential of the Linglong gold deposit, Jiaodong Peninsula: Geochemical comparison of ore fluids. Ore Geol. Rev. 120, 103434. https://doi.org/10.1016/j.oregeorev.2020.103434.

Guo, L.N., Goldfarb, R.J., Wang, Z.L., Li, R.H., Chen, B.H., Li, J.L., 2017. A comparison of Jiaojia-and Linglong-type gold deposit ore-forming fluids: do they differ? Ore Geol. Rev. 88, 511–533.

He, D.Y., Qiu, K.F., Yu, H.C., Huang, Y.Q., Ding, Z.J., Shen, Y., 2020. Petrogenesis of the Early Cretaceous trachy-dacite from Mashan in the Jiaolai Basin. North China Craton. Acta Petrol. Sin. 36, 3705–3720.

Hetherington, C.J., Harlov, D.E., 2008. Metasomatic thorite and uraninite inclusions in xenotime and monazite from granitic pegmatites, Hidra anorthosite massif, southwestern Norway: Mechanics and fluid chemistry. Am. Mineral. 93 (5-6), 806–820.

Hu, F.F., Fan, H.R., Jiang, X.H., Li, X.C., Yang, K.F., Mernagh, T., 2013. Fluid inclusions at different depths in the Sanshandao gold deposit, Jiaodong Peninsula, China. Geofluids 13 (4), 528–541.

Huang, T., Yang, L., Liu, X., Li, H., Zhang, B., Wang, J., Zhao, Y., Zhang, N., 2014. Crustal evolution of the Jiaobei terrane: Evidence from U-Pb ages, trace element compositions and Hf isotopes of inherited zircons of the Linglong biotite granite. Acta Petrol. Sin. 30, 2574–2594.

Jerram, D.A., Dobson, K.J., Morgan, D.J., Pankhurst, M.J., 2018. The Petrogenesis of Magmatic Systems: Using Igneous Textures to Understand Magmatic Processes, Volcanic and Igneous Plumbing Systems. Elsevier 191–229.

Kusiak, M.A., Dunkley, D.J., Whitehouse, M.J., Wilde, S.A., Sałacińska, A., Konečný, P., Szopa, K., Gawęda, A., Chew, D., 2018. Peak to post-peak thermal history of the Saglek Block of Labrador: A multiphase and multi-instrumental approach to geochronology. Chem. Geol. 484, 210–223.

Li, W., Yang, Z., Chiaradia, M., Lai, Y., Yu, C., Zhang, J., 2020. Redox state of southern Tibetan upper mantle and ultrapotassic magmas. Geology 48, 733–736.

Li, X.C., Harlov, D.E., Zhou, M.F., Hu, H., 2021. Experimental investigation into the disturbance of the Sm-Nd isotopic system during metasomatic alteration of apatite. Geochim. Cosmochim. Acta.

Li, X.H., Fan, H.R., Hu, F.F., Hollings, P., Yang, K.F., Liu, X., 2019. Linking lithospheric thinning and magmatic evolution of late Jurassic to early cretaceous granitoids in the Jiaobei Terrane, southeastern North China Craton. Lithos 324, 280–296.

Liu, C., Zhu, G., Zhang, S., Gu, C., Li, Y., Su, N., Xiao, S., 2018. Mesozoic strike-slip movement of the Dunhua-Mishan Fault Zone in NE China: A response to oceanic plate subduction. Tectonophysics 723, 201–222.

Liu, D., Zhao, Z., Zhu, D.-C., Niu, Y., Harrison, T.M., 2014. Zircon xenocrysts in Tibetan ultrapotassic magmas: imaging the deep crust through time. Geology 42, 43–46.

Liu, X., Fan, H.R., Evans, N.J., Yang, K.F., Danišík, M., McInnes, B.I., Qin, K.Z., Yu, X.F., 2017. Exhumation history of the Sanshandao Au deposit, Jiaodong: constraints from structural analysis and (U-Th)/He thermochronology. Scient. Rep. 7, 1–12.

Lu, Y.H., Zhao, Z.F., Zheng, Y.F., 2016. Geochemical constraints on the source nature and melting conditions of Triassic granites from South Qinling in central China. Lithos 264, 141–157.

Ludwig, K., 2012. Isoplot 3.75. A Geochronological toolkit for Microsoft Excel. Berkeley Geochronology Center, Spec. Pub. 5.

Ma, F., Sun, Z., Sun, Z., Lu, R., Gu, H., Guo, J., Cai, X., 2017. Temperature measurement used for 4000-m depth drilling and geothermal characteristics in Jiaodong Peninsula, China. Environ. Earth Sci. 76, 1–10.

Meisel, T., Walker, R.J., Irving, A.J., Lorand, J.-P., 2001. Osmium isotopic compositions of mantle xenoliths: a global perspective. Geochim. Cosmochim. Acta 65, 1311–1323.

Mills, S.E., Tomkins, A.G., Weinberg, R.F., Fan, H.R., 2015. Implications of pyrite geochemistry for gold mineralisation and remobilisation in the Jiaodong gold district, northeast China. Ore Geol. Rev. 71, 150–168.

O'Sullivan, G., Chew, D., Kenny, G., Henrichs, I., Mulligan, D., 2020. The trace element composition of apatite and its application to detrital provenance studies. Earth Sci. Rev. 201, 103044.

O'Sullivan, G.J., Chew, D.M., 2020. The clastic record of a Wilson Cycle: Evidence from detrital apatite petrochronology of the Grampian-Taconic fore-arc. Earth Planet. Sci. Lett. 552, 116588.

Odlum, M.L., Stockli, D.F., 2020. Geochronologic constraints on deformation and metasomatism along an exhumed mylonitic shear zone using apatite U-Pb, geochemistry, and microtextural analysis - ScienceDirect. Earth Planet. Sci. Lett. 538, 116177.

Qiu, K.F., Deng, J., Yu, H.C., Wu, M.Q., Wang, Y., Zhang, L., Goldfarb, R., 2021a. Identifying hydrothermal quartz vein generations in the Taiyangshan porphyry Cu-Mo deposit (West Qinling, China) using cathodoluminescence, trace element geochemistry, and fluid inclusions. Ore Geol. Rev., 103882.

Qiu, K.F., Goldfarb, R., Deng, J., Yu, H.C., Gou, Z.Y., Ding, Z.J., Wang, Z.K., Li, D.P., 2020a. Gold Deposits of the Jiaodong Peninsula, Eastern China. In: Sillitoe, R.H., Goldfarb, R., Robert, F., Simmons, S.F. (Eds.), Geology of the World's Major Gold Deposits and Provinces. Society of Economic Geologists, Littleton, pp. 753–773.

Qiu, K.F., Yu, H.C., Deng, J., McIntire, D., Gou, Z.Y., Geng, J.Z., Chang, Z.S., Zhu, R., Li, K.N., Goldfarb, R., 2020b. The giant Zaozigou Au-Sb deposit in West Qinling, China: magmatic- or metamorphic-hydrothermal origin? Mineral. Deposita 55, 345–362.

Qiu, K.F., Yu, H.C., Hetherington, C., Huang, Y.Q., Yang, T., Deng, J., 2021b. Tourmaline composition and boron isotope signature as a tracer of magmatic-hydrothermal processes. Am. Mineral. 106, 1033–1044.

Qiu, K.F., Yu, H.C., Wu, M.Q., Geng, J.Z., Ge, X.K., Gou, Z.Y., Taylor, R.D., 2019. Discrete Zr and REE mineralization of the Baerzhe rare-metal deposit. China. Am. Mineral. 104, 1487–1502.

Qiu, N., Zuo, Y., Chang, J., Li, W., 2014. Geothermal evidence of Meso-Cenozoic lithosphere thinning in the Jiyang sub-basin, Bohai Bay Basin, eastern North China Craton. Gondwana Res. 26, 1079–1092.

Quan, Y.K., Yang, D.B., Mu, M.S., Hao, L.R., Yang, H.T., Wang, A.Q., Xu, W.L., 2020. Tectonic evolution of the northeastern North China Craton: Constraints from geochronology and Sr–Nd–Hf–O isotopic data from Late Triassic intrusive rocks on Liaodong Peninsula, NE China. Lithos 362, 105489.

Ren, Z., Qi, K., Liu, R., Cui, J., Chen, Z., Zhang, Y., Yang, G., Ma, Q., 2020. Dynamic background of Early Cretaceous tectonic thermal events and its control on various

mineral accumulations such as oil and gas in the Ordos Basin. Acta Petrol. Sinica 36, 1213–1234.
Sai, S.X., Deng, J., Qiu, K.F., Miggins, D.P., Zhang, L., 2020. Textures of auriferous quartz-sulfide veins and 40Ar/39Ar geochronology of the Rushan gold deposit: Implications for processes of ore-fluid infiltration in the eastern Jiaodong gold province. China. Ore Geol. Rev. 117, 103254.
Sai, S.X., Zhao, T.M., Wang, Z.L., Huang, S.Y., Zhang, L., 2016. Petrogenesis of Linglong biotite granite; Constraints from mineralogical characteristics. Acta Petrol. Sin. 32, 2477–2493.
Siebel, W., Schmitt, A.K., Danišík, M., Chen, F., Meier, S., Weiß, S., Eroğlu, S., 2009. Prolonged mantle residence of zircon xenocrysts from the western Eger rift. Nat. Geosci. 2, 886–890.
Sláma, J., Košler, J., Condon, D.J., Crowley, J.L., Gerdes, A., Hanchar, J.M., Horstwood, M.S., Morris, G.A., Nasdala, L., Norberg, N., 2008. Plešovice zircon—a new natural reference material for U-Pb and Hf isotopic microanalysis. Chem. Geol. 249, 1–35.
Stacey, J.t., Kramers, J., 1975. Approximation of terrestrial lead isotope evolution by a two-stage model. Earth Planet. Sci. Lett. 26, 207–221.
Szopa, K., Sałacińska, A., Gumsley, A.P., Chew, D., Petrov, P., Gawęda, A., Zagórska, A., Deput, E., Gospodinov, N., Banasik, K., 2020. Two-Stage Late Jurassic to Early Cretaceous Hydrothermal Activity in the Sakar Unit of Southeastern Bulgaria. Minerals 10, 266.
Tapster, S., Roberts, N., Petterson, M., Saunders, A., Naden, J., 2014. From continent to intra-oceanic arc: Zircon xenocrysts record the crustal evolution of the Solomon island arc. Geology 42, 1087–1090.
Wang, H., Yang, L.Q., Wang, S.R., Zhang, L., Wei, Y.J., Lu, G.Y., 2020. The process of rubefication and its relationship with gold mineralization of Sizhuang gold deposit, northwestern Jiaodong Peninsula, eastern China. Acta Petrol. Sin. 36, 1515–1528.
Wang, Y., Qiu, K.F., Müller, A., Hou, Z.L., Zhu, Z.H., Yu, H.C., 2021. Machine Learning Prediction of Quartz Forming-Environments. J. Geophys. Res. Solid Earth 126.
Wen, B.J., Fan, H.R., Hu, F.F., Liu, X., Yang, K.F., Sun, Z.F., Sun, Z.F., 2016. Fluid evolution and ore genesis of the giant Sanshandao gold deposit, Jiaodong gold province, China: Constrains from geology, fluid inclusions and H-O–S–He–Ar isotopic compositions. J. Geochem. Explor. 171, 96–112.
Wen, B.J., Fan, H.R., Santosh, M., Hu, F.F., Pirajno, F., Yang, K.F., 2015. Genesis of two different types of gold mineralization in the Linglong gold field, China: constrains from geology, fluid inclusions and stable isotope. Ore Geol. Rev. 65, 643–658.
Whitney, D.L., Evans, B.W., 2010. Abbreviations for names of rock-forming minerals. Am. Mineral. 95, 185–187.
Wiedenbeck, M., Alle, P., Corfu, F., Griffin, W., Meier, M., Oberli, F.v., Quadt, A.v., Roddick, J., Spiegel, W., 1995. Three natural zircon standards for U-Th-Pb, Lu-Hf, trace element and REE analyses. Geostand. Newslett. 19, 1–23.
Xie, S., Wu, Y., Zhang, Z., Qin, Y., Liu, X., Wang, H., Qin, Z., Liu, Q., Yang, S., 2012. U-Pb ages and trace elements of detrital zircons from Early Cretaceous sedimentary rocks in the Jiaolai Basin, north margin of the Sulu UHP terrane: Provenances and tectonic implications. Lithos 154, 346–360.
Xu, H., Zhang, J., Wang, Y., Liu, W., 2016. Late Triassic alkaline complex in the Sulu UHP terrane: Implications for post-collisional magmatism and subsequent fractional crystallization. Gondwana Res. 35, 390–410.
Yang, K.F., Jiang, P., Fan, H.R., Zuo, Y.B., Yang, Y.H., 2018. Tectonic transition from a compressional to extensional metallogenic environment at~ 120 Ma revealed in the Hushan gold deposit, Jiaodong, North China Craton. J. Asian Earth Sci. 160, 408–425.
Yang, L.Q., Deng, J., Dilek, Y., Qiu, K.F., Ji, X.Z., Li, N., Taylor, R.D., Yu, J.Y., 2015. Structure, geochronology, and petrogenesis of the Late Triassic Puziba granitoid dikes in the Mianlue suture zone, Qinling orogen. China. Geol. Soc. Am. Bull. 127, 1831–1854.
Yang, L.Q., Deng, J., Wang, Z.L., Zhang, L., Goldfarb, R.J., Yuan, W.M., Weinberg, R.F., Zhang, R.Z., 2016. Thermochronologic constraints on evolution of the Linglong Metamorphic Core Complex and implications for gold mineralization: A case study from the Xiadian gold deposit, Jiaodong Peninsula, eastern China. Ore Geol. Rev. 72, 165–178.
Yu, H.C., Qiu, K.F., Hetherington, C.J., Chew, D., Huang, Y.Q., He, D.Y., Geng, J.Z., Xian, H.Y., 2021a. Apatite as an alternative petrochronometer to trace the evolution of magmatic systems containing metamict zircon. Contrib. Mineral. Petrol. 176.
Yu, H.C., Qiu, K.F., Nassif, M.T., Geng, J.Z., Sai, S.X., Duo, D.W., Huang, Y.Q., Wang, J., 2020. Early orogenic gold mineralization event in the West Qinling related to closure of the Paleo-Tethys Ocean-Constraints from the Ludousou gold deposit, central China. Ore Geol. Rev. 117, 103217.
Yu, H.C., Qiu, K.F., Pirajno, F., Zhang, P.C., Dong, W.Q., 2021b. Revisiting Phanerozoic evolution of the Qinling Orogen (East Tethys) with perspectives of detrital zircon. Gondwana Res., doi.org/10.1016/j.gr.2021.1010.1022.
Zeng, L.P., Zhao, X.F., Li, X.C., Hu, H., McFarlane, C., 2016. In situ elemental and isotopic analysis of fluorapatite from the Taocun magnetite-apatite deposit, Eastern China: Constraints on fluid metasomatism. Am. Mineral. 101, 2468–2483.
Zhang, L., Groves, D.I., Yang, L.Q., Wang, G.W., Liu, X.D., Li, D.P., Song, Y.X., Shan, W., Sun, S.C., Wang, Z.K., 2020a. Relative roles of formation and preservation on gold endowment along the Sanshandao gold belt in the Jiaodong gold province, China: importance for province-to district-scale gold exploration. Mineral. Deposita 55, 325–344.
Zhang, L., Weinberg, R.F., Yang, L.Q., Groves, D.I., Sai, S.X., Matchan, E., Phillips, D., Kohn, B.P., Miggins, D.P., Liu, Y., 2020b. Mesozoic orogenic gold mineralization in the Jiaodong Peninsula, China: a focused event at 120±2 Ma during cooling of pregold granite intrusions. Econ. Geol. 115, 415–441.
Zhao, Y., Wu, Y., He, Y., Liu, X., 2020. Refining the timing and mechanism of the Triassic partial melting in the Sulu UHP orogen, China: Zircon and garnet evidence from a felsic vein and its host granitic gneiss. Lithos 352, 105264.
Zhao, Z.F., Liu, Z.B., Chen, Q., 2017. Melting of subducted continental crust: Geochemical evidence from Mesozoic granitoids in the Dabie-Sulu orogenic belt, east-central China. J. Asian Earth Sci. 145, 260–277.